Medical Image Analysis 82 (2022) 102579

Contents lists available at ScienceDirect

Medical Image Analysis

journal homepage: www.elsevier.com/locate/media

uFLIM — Unsupervised analysis of FLIM-FRET microscopy data

Francesco Masia [a,b,*], Walter Dewitte [b], Paola Borri [b], Wolfgang Langbein [a]

[a] School of Physics and Astronomy, Cardiff University, The Parade, Cardiff CF24 3AA, UK
[b] School of Biosciences, Cardiff University, Museum Avenue, Cardiff CF10 3AX, UK

ARTICLE INFO

MSC:
62H35

Keywords:
Fluorescence lifetime imaging
Förster resonant energy transfer
Non-negative matrix factorization

ABSTRACT

Despite their widespread use in cell biology, fluorescence lifetime imaging microscopy (FLIM) data-sets are challenging to analyse, because each spatial position can contain a superposition of multiple fluorescent components. Here, we present a data analysis method employing all information in the available photon budget, as well as being fast. The method, called uFLIM, determines spatial distributions and temporal dynamics of multiple fluorescent components with no prior knowledge. It goes significantly beyond current approaches which either assume the functional dependence of the dynamics, e.g. an exponential decay, or require dynamics to be known, or calibrated. Its efficient non-negative matrix factorization algorithm allows for real-time data processing. We validate *in silico* that uFLIM is capable to disentangle the spatial distribution and spectral properties of five fluorescing probes, from only two excitation and detection channels and a photon budget of 100 detected photons per pixel. By adapting the method to data exhibiting Förster resonant energy transfer (FRET), we retrieve the spatial and transfer rate distribution of the bound species, without constrains on donor and acceptor dynamics.

1. Introduction

Fluorescence microscopy is a widely used tool to study the distribution of biomolecules in living cells and tissues, with high contrast, specificity, and spatial resolution. The decay dynamics of the fluorescence intensity following pulsed excitation can reveal information on the local environment of the emitting fluorophore. This concept is used in fluorescence lifetime imaging microscopy (FLIM), where spatially-resolved emission dynamics are recorded (Berezin and Achilefu, 2010). Typically, the emission intensity is measured as a function of the delay after an excitation pulse, but there are also frequency-domain implementations (Raspe et al., 2016). Spatially-resolved fluorescence dynamics have been used to sense local variation of temperature (Okabe et al., 2012), pH (Orte et al., 2013; Schmitt et al., 2014), and ion concentration (Agronskaia et al., 2004). FLIM can also be used to distinguish multiple spectrally overlapping fluorophores via their different decay dynamics (Niehörster et al., 2016).

Among the various processes which alter the lifetime of an emitter, Förster resonant energy transfer (FRET) offers the possibility of studying protein–protein interaction (Sun et al., 2011; Margineanu et al., 2016). Here, two proteins of interest are tagged with different fluorophores, called donor and acceptor. The emission spectrum of the donor spectrally overlaps with the absorption spectrum of the acceptor, and the excitation is spectrally overlapping with the absorption of the donor. If the distance of the two fluorophores is small enough, typically in the nanometre range, significant non-radiative transfer of the excitation occurs from the donor to the acceptor. Such energy transfer can be detected by a quenching of the donor emission and a corresponding enhancement of the acceptor emission. For high accuracy and sensitivity, a method to detect the transfer not relying on absolute intensities is preferable, and this can be achieved by measuring the change of the fluorescence dynamics in FLIM. The energy transfer provides an additional loss channel for the donor, increasing its decay rate, and a corresponding delayed excitation of the acceptor. Notably, FLIM-FRET is not affected by absolute intensity changes, typically present due to photobleaching, illumination inhomogeneity and/or concentration distributions.

To analyse FLIM, a common approach is to fit the signal decay assuming a mono- or bi-exponential decay behaviour. Recently, global analysis methods offering faster algorithms compared to pixel by pixel fitting have been reported (Datta et al., 2020), and a clustering step can be introduced to further speed up the analysis (Brodwolf et al., 2020; Li et al., 2021). Most of these methods assume exponential decay dynamics, and the instrument response function in time-domain needs to be known to extract the exponential time constants. FRET is observed as an additional decay rate and can be extracted from the fit parameters (Laptenok et al., 2007; Warren et al., 2013). However, while being a convenient mathematical function to use, and the simplest solution

---

* Corresponding author at: School of Biosciences, Cardiff University, Museum Avenue, Cardiff CF10 3AX, UK.
E-mail addresses: masiaf@cf.ac.uk (F. Masia), dewittew@cf.ac.uk (W. Dewitte), borrip@cf.ac.uk (P. Borri), langbeinww@cf.ac.uk (W. Langbein).

https://doi.org/10.1016/j.media.2022.102579
Received 8 December 2021; Received in revised form 24 May 2022; Accepted 11 August 2022

of rate equation models, an exponential decay is only approximately representing the physical behaviour of a fluorophore embedded in a heterogeneous environment.

Phasor analysis is an alternative simple and widely used approach (Clayton et al., 2004; Digman et al., 2008; Stringari et al., 2011). In this method, each FLIM pixel is represented by two quantities, namely the real and imaginary part of the Fourier coefficient of the first harmonic (typically referring to the excitation repetition rate) normalized to the amplitude of the zeroth harmonic. These values are then interpreted as coordinates in the resulting "phasor plot" in the complex plane. Pure exponential decay dynamics of varying decay times are forming a semi-circle in this plot. Due to the linearity of the transform, mixed exponential decay dynamics are resulting in averages of pure component phasors, and thus have amplitudes inside the circle. The phasor analysis provides a useful tool when applied to FLIM-FRET data. The occurrence of energy transfer can be identified as a deviation of the phasors from the values obtained in regions of the sample occupied only by unbound donor molecules. For a quantitative analysis of FRET some assumptions are imposed, e.g. the FRET efficiency trajectory is obtained by approximating the unbound donor fluorescence as mono-exponential.

FLIM data can also be analysed by linear unmixing of the intensity decay on the basis of selected reference patterns (Gregor and Patting, 2015) measured *a priori* in samples with similar properties as the sample under investigation. In this method, each fluorescence decay is approximated as a linear combination of reference decay curves by minimizing the Kullback–Leibler discrepancy (KLD) (Lee and Seung, 2001), which maximizes the likelihood of the model for data showing Poisson noise, which is the expected photon detection statistics. Typically, a gradient descent method using multiplicative update rules is used to find the non-negative fractional concentrations of the reference patterns (Lee and Seung, 2001). The reference patterns are either extracted from singly labelled control samples or by selecting regions of the image which are assumed to show the individual components. This approach has been applied to the analysis of multispectral time-domain FLIM, and up to nine different fluorophores could be visualized (Niehörster et al., 2016). The supervised determination of the components and their dynamics complicates the analysis, and introduces a bias. Specifically in the analysis of FRET-FLIM data, where the different components interact, a reliable determination of the individual component dynamics is challenging.

Recently, a deep learning method to analyse FLIM and FLIM-FRET datasets was developed (Smith et al., 2019). However, the benefits of the fit-free approach are accompanied by the typical shortcoming of deep learning, i.e. the need to generate the training set and to train the neural network, which is a topic of further investigation (Xiao et al., 2021). Notably, generating the training dataset requires prior knowledge. For example, in Smith et al. (2019) a single or bi-exponential fluorescence decay and the instrument response were used to create the training set, which is defining the expected responses, and restricting the retrieved parameters to two time-constants and two amplitudes.

In this work, we propose an unsupervised FLIM analysis (uFLIM) method, using a fast non-negative matrix factorization (NMF) algorithm (Kim and Park, 2009) and random initial guesses for both the spatial distribution and decay traces of the factorization components. Similar to the pattern unmixing, the NMF method decomposes the data into a linear combination of few components, but differently from pattern unmixing, it does not require prior knowledge of the component patterns, which instead can be deduced as part of the factorization. The method thus offers the advantages of pattern unmixing, *i.e.* the absence of assumptions on fluorescence dynamics and of prior knowledge of the instrument response function, while operating at higher speed and additionally dropping the prior knowledge of reference patterns. We demonstrate the performance of uFLIM in distinguishing multiple spectrally overlapping fluorescing proteins, showing that the method can retrieve the spatial distribution and dynamics of five fluorescent protein probes using data from a simple FLIM set-up with only two excitation lasers and two detection channels.

Building on this method, we introduce a FRET analysis, which uses the donor and acceptor dynamics determined by uFLIM from samples or sample regions not showing FRET. Energy transfer is quantitatively characterized by the quantum efficiencies of donor and acceptor emission into the detection channels, as well as the mean and variance of the transfer rate distribution, here assumed to be log-normal (Balakrishnan et al., 1994). The analysis determines the values of these quantities, and thus the donor–acceptor pair (DAP) dynamics, together with the spatial distribution of the DAPs, by minimizing the NMF factorization error. Other components, such as autofluorescence, can be retrieved at the same time without prior knowledge. Notably, uFLIM-FRET does not assume a functional dependence of the fluorescence dynamics, but calculates the non-exponential donor and acceptor dynamics in the DAP from their unbound dynamics using the distribution of FRET rates.

2. Method

2.1. uFLIM

Measured FLIM data are reshaped as an $(N_\mathrm{s}{\times}N_\mathrm{t})$ matrix $\mathbf{D}$ where N_s and N_t indicate the number of spatial and temporal points, respectively. Then, a number of components N_c much smaller than N_t is chosen to represent the data, and NMF is used to determine the spatial distribution matrix $\mathbf{S}$ of $N_\mathrm{s}{\times}N_\mathrm{c}$ elements, and the dynamics matrix $\mathbf{T}$ of $N_\mathrm{c}{\times}N_\mathrm{t}$ elements. If present, multiple spectral channels are stacked in the N_t dimension, and multiple data are stacked in the N_s dimension, keeping track of the ordering for later decomposition.

We assume in the following that $\mathbf{D}$ is given as the number of detected photons, which has Poissonian noise with a standard deviation given by $\sqrt{D_{ij}}$. We utilize a fast NMF algorithm that minimizes the residual $\|\mathbf{D}-\mathbf{ST}\|_2$, where $\|.\|_2$ indicates the Frobenius norm (Kim and Park, 2009). This method provides the decomposition of maximum likelihood in the case of Gaussian white noise in the data, i.e. a noise independent of the data value. To be able to use this algorithm, which is 2–3 orders of magnitude faster than gradient descent methods accounting for non-white noise, we partially whiten the data before factorization by applying a scaling as follows. We generate the time-averaged image $\bar{\mathbf{S}}$ and the spatially averaged dynamics $\bar{\mathbf{T}}$ by averaging $\mathbf{D}$ along the temporal and spatial points, respectively,

$$\bar{S}_i = \frac{1}{N_\mathrm{t}}\sum_j D_{ij}, \quad \bar{T}_j = \frac{1}{N_\mathrm{s}}\sum_i D_{ij}, \tag{1}$$

For average counts below unity, the photon counting statistics deviates significantly from Gaussian noise, and the above whitening is not representing the required whitening well. We therefore limit $\bar{S}_i$ and $\bar{T}_j$ to a minimum of ξ in the whitening. The background-subtracted, partially whitened data $\mathbf{D}^\mathrm{w}$ are then defined as

$$D^\mathrm{w}_{ij} = \frac{D_{ij}-b}{\sqrt{\bar{S}_i}\sqrt{\bar{T}_j}}\,, \tag{2}$$

with the average dark counts b, which can be measured independently. We assume here that b is equal across the position, time, and spectral channels, as it is typically the case for scanning time-correlated single photon counting, but also note that inhomogeneous dark counts can be subtracted in the same fashion. In $\mathbf{D}^\mathrm{w}$, the data has been divided by the expected standard deviation of the data when factorized into the average spatial and temporal dependence. This method whitens spatially dependent time-integrated intensities, as well as spatially integrated time-dependent intensities. $\mathbf{D}^\mathrm{w}$ is then factorized by NMF, minimizing $E = \|\mathbf{D}^\mathrm{w} - \mathbf{S}^\mathrm{w}\mathbf{T}^\mathrm{w}\|_2$, and the resulting decomposition $\mathbf{S}^\mathrm{w}$ and $\mathbf{T}^\mathrm{w}$ is de-whitened to recover the factorization of the original data

$$S_{ij} = S^\mathrm{w}_{ij}\sqrt{\bar{S}_i}\,, \quad T_{ij} = T^\mathrm{w}_{ij}\sqrt{\bar{T}_j}\,, \tag{3}$$

so that $\mathbf{D} \approx \mathbf{ST} + b$. We will see that this treatment of noise is providing equivalent results to minimizing the KLD for the data considered. When showing $\mathbf{S}$ in this work, it refers to a normalized $\mathbf{T}$, such that $\mathbf{S}$ represents the number of photons detected at each spatial point.

2.2. uFLIM-FRET

Beyond the unsupervised analysis of FLIM data, we have extended the algorithm to retrieve the spatial distribution of FRET pairs. In the literature, FRET efficiencies are often derived from fitting the measured dynamics by exponential decays and comparing the resulting decay times with the decay constant measured in samples where only the donor is present. These methods are limited by the assumption of exponential decay dynamics, and require the knowledge of the instrument response function.

In uFLIM, the temporal dynamics are retrieved without prior knowledge or assumption of an exponential decay. Therefore uFLIM can be applied to data showing pure donor and acceptor dynamics as components, providing the normalized pure donor and acceptor dynamics, which we call $\mathbf{T}^{\rm d}$ and $\mathbf{T}^{\rm a}$, with $\{\mathbf{T}^{\rm d}\} = \{\mathbf{T}^{\rm a}\} = 1$ where $\{.\}$ indicates the 1-norm. We note that the emission of a molecule is proportional to the probability to be in its excited state. FRET occurs when donor and acceptor are in close proximity, forming a DAP. The FRET process introduces a non-radiative excitation transfer channel from the donor to the acceptor, characterized by a rate γ (a sketch of the energy diagram is shown in the supplementary information (SI) Fig. S25). Therefore, the fluorescence intensity of the donor in the DAP at a given time point can be calculated by subtracting from $\mathbf{T}^{\rm d}$ the FRET to the acceptor up to that time point. Equivalently, the intensity of the acceptor in the DAP can be calculated from $\mathbf{T}^{\rm a}$ by adding the FRET from the donor. The modified donor dynamics $\tilde{\mathbf{T}}^{\rm d}$ in the DAP is accordingly calculated using

$$\tilde{T}^{\rm d}_i(\gamma) = T^{\rm d}_i - \sum_{j=1}^{i-1} f_j(\gamma)\hat{T}^{\rm d}_{i-j+1}\,, \tag{4}$$

iterating along the time point $i = 1, 2, \dots, l$. This expression contains the dynamics

$$\hat{T}^{\rm d}_k = \begin{cases} T^{\rm d}_{m+k-1}/T^{\rm d}_m & \text{for } k \le l-m+1 \\ \hat{T}^{\rm d}_{l-m} T^{\rm d}_l / T^{\rm d}_{2l-m-k} & \text{for } k > l-m+1 \end{cases}, \tag{5}$$

where m is the time point at which $\mathbf{T}^{\rm d}$ is maximum. In Eq. (5), we have extrapolated the donor excitation decay beyond the last measured point l using the decay observed over the extrapolation time interval prior to l. The FRET transfer $f_j(\gamma)$ at time j over the time step Δ is given by

$$f_j(\gamma) = \tilde{T}^{\rm d}_j \gamma \Delta\,, \tag{6}$$

using the modified occupation $\tilde{T}^{\rm d}_j$ of the donor excited state at that time and the transfer rate γ.

These equations determine the effect of FRET on the donor excitation, by subtracting the FRET transfer at points in the past, propagated to the present using the response function $\hat{\mathbf{T}}^{\rm d}$. We approximate $\hat{\mathbf{T}}^{\rm d}$ by the measured donor emission dynamics, normalized to its maximum and starting from its maximum as time zero of the response. This is adequate for FRET rates smaller than the inverse time resolution of the measurements, and is consistent with the finite resolution of the data for which it is used. To support this statement, we have compared the resulting dynamics with the analytical solution of the donor excitation modified by a single FRET process in the simple condition of a mono-exponential decay for the pure donor and a Gaussian instrument response function (IRF), as shown in the SI Sec. S6. The time-resolution limitation can be controlled by refining the system dynamics, for example, by deconvolution of a response function before analysis. Note, however, that the deconvolution is modifying the noise of the data from the simple Poisson distribution of photon counts.

Fig. 1 illustrates the iterative calculation of $\tilde{\mathbf{T}}^{\rm d}$ from $\mathbf{T}^{\rm d}$ by Eq. (4). The modified dynamics $\tilde{\mathbf{T}}^{\rm d}(n)$ including only the contributions of previous time points up to $n-1$ are shown in green filled circles and are given by

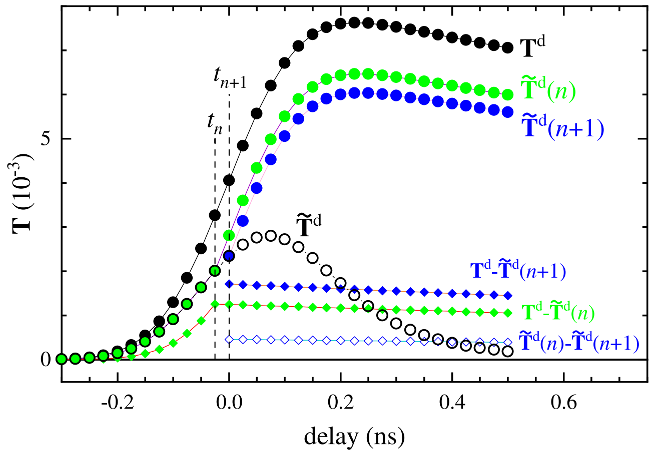

Fig. 1. Illustration of Eq. (4) calculating the modified donor dynamics in the DAP undergoing FRET, $\tilde{\mathbf{T}}^{\rm d}$, from the free donor dynamics $\mathbf{T}^{\rm d}$. Intermediate results subtracting only the transfer occurring before time point n ($\tilde{\mathbf{T}}^{\rm d}(n)$) and $n+1$ ($\tilde{\mathbf{T}}^{\rm d}(n+1)$) are shown, together with the corresponding subtracted transfer $\mathbf{T}^{\rm d} - \tilde{\mathbf{T}}^{\rm d}(n)$ and $\mathbf{T}^{\rm d} - \tilde{\mathbf{T}}^{\rm d}(n+1)$, and the additional transfer occurring between t_n and t_{n+1}, given by $\tilde{\mathbf{T}}^{\rm d}(n) - \tilde{\mathbf{T}}^{\rm d}(n+1)$. The curves are simulated for a donor decay rate of 0.33/ns, a log-normal FRET rate distribution Eq. (13) with $\bar{\gamma} = 10$/ns and $\sigma = 0.5$, using a time step of $\Delta = 25$ ps and a Gaussian IRF of width $s = 100$ ps (see SI Sec. S6).

$$\tilde{T}^{\rm d}_i(n) = T^{\rm d}_i - \sum_{j=1}^{\min(n,i)-1} f_j \hat{T}^{\rm d}_{i-j+1}. \tag{7}$$

Including the time point n, the resulting $\tilde{\mathbf{T}}^{\rm d}(n+1)$ (blue filled circles) is decreased for $i > n$ by the contribution of the excitation transferred between the time point n and $n+1$ (empty blue diamonds), given by

$$\tilde{T}^{\rm d}_i(n) - \tilde{T}^{\rm d}_i(n+1) = \begin{cases} f_n \hat{T}^{\rm d}_{i-n+1}, & \text{for } i \ge n \\ 0 & \text{otherwise} \end{cases}. \tag{8}$$

Including all previous time points, we recover the modified donor dynamics $\tilde{\mathbf{T}}^{\rm d}$.

The modified acceptor excitation dynamics are calculated using the same approach, resulting in

$$\tilde{T}^{\rm a}_i(\gamma) = \kappa T^{\rm a}_i + \sum_{j=1}^{i-1} f_j(\gamma)\hat{T}^{\rm a}_{i-j+1}, \tag{9}$$

with the normalized and zero-centred acceptor dynamics

$$\hat{T}^{\rm a}_k = \begin{cases} T^{\rm a}_{m+k-1}/T^{\rm a}_m & \text{for } k \le l-m+1 \\ \hat{T}^{\rm a}_{l-m} T^{\rm a}_l / T^{\rm a}_{2l-m-k} & \text{for } k > l-m+1 \end{cases}. \tag{10}$$

The normalization of $\mathbf{T}^{\rm d}$ and $\mathbf{T}^{\rm a}$ ensures the conservation of the number of excitations by the transfer from donor to acceptor in Eq. (9), which also contains the direct excitation of the acceptor by the laser (see SI Fig. S25) quantified by κ. While κ can be included in the parameters to be determined by the method, we assume in the following that κ is known *a priori*, noting that it is given by the relative absorption cross-section of acceptor and donor at the excitation wavelength and can be determined independently. We assume to have two spectral channels, and that the donor and acceptor emission is detected dominantly by the respective channels, given by the fraction of donor $R^{\rm d}$ (acceptor $R^{\rm a}$) emission detected by the donor (acceptor) channel, respectively. The dynamics $\tilde{\mathbf{T}}^{\rm D}$ ($\tilde{\mathbf{T}}^{\rm A}$) detected in the donor (acceptor) channel for a DAP undergoing FRET with rate γ is then given by

$$\begin{aligned} \tilde{\mathbf{T}}^{\rm D}(\gamma, q) &= R^{\rm d}\tilde{\mathbf{T}}^{\rm d}(\gamma) + q\left(1 - R^{\rm a}\right)\tilde{\mathbf{T}}^{\rm a}(\gamma)\,, \\ \tilde{\mathbf{T}}^{\rm A}(\gamma, q) &= \left(1 - R^{\rm d}\right)\tilde{\mathbf{T}}^{\rm d}(\gamma) + qR^{\rm a}\tilde{\mathbf{T}}^{\rm a}(\gamma)\,. \end{aligned} \tag{11}$$

Here, we have introduced the ratio q between acceptor and donor, of the detection probability (summed over both channels) of an excitation decay, to take into account the different quantum efficiency of the acceptor and donor, and the different probability of detecting an emitted photon in the two channels, including detector efficiency and filter performance. The values of R^{d} and R^{a} can be simply measured using samples of only donor or acceptor from the ratio of the number of detected photons in donor versus acceptor channel. Determining q instead requires to additionally determine the relative excitation rates of the donor versus acceptor molecules in the two samples, which in turn requires knowledge of relative molar concentration and relative absorption κ. We have considered here the case where R^{d} and R^{a} have been measured, while q is determined by uFLIM-FRET.

Typically, the acceptor has a small absorption at the excitation wavelength, so $\kappa \ll 1$, and is hardly detected by the donor channel, so $1 - R^{\mathrm{a}} \ll 1$. In the simulations shown later we use the more challenging condition of $\kappa = 1$, where three components (donor, acceptor, and DAP) need to be included, while the simpler case $\kappa = 0$, showing an improved retrieval for a given photon budget, is given in the SI.

In the NMF, the temporal points of the donor and acceptor channel are concatenated into the temporal dimension of $\mathbf{D}$. Three NMF components in $\mathbf{T}$ are used, given by the donor, $\left[R^{\mathrm{d}}\mathbf{T}^{\mathrm{d}}, \left(1 - R^{\mathrm{d}}\right)\mathbf{T}^{\mathrm{d}}\right]$, the acceptor $\kappa q\left[(1 - R^{\mathrm{a}})\,\mathbf{T}^{\mathrm{a}}, R^{\mathrm{a}}\mathbf{T}^{\mathrm{a}}\right]$ and the DAP $\tilde{\mathbf{T}}^{\mathrm{f}}(\gamma, q) = \left[\tilde{\mathbf{T}}^{\mathrm{D}}(\gamma, q), \tilde{\mathbf{T}}^{\mathrm{A}}(\gamma, q)\right]$. The latter is a function of the FRET rate γ and the ratio q. The spatial distributions $\mathbf{S}^{\mathrm{d}}$, $\mathbf{S}^{\mathrm{a}}$, and $\mathbf{S}^{\mathrm{f}}$ of these components are determined from the data by NMF. Additional components can be added to the NMF analysis, for example, to take into account autofluorescence, determining their temporal dynamics and spatial distribution without prior knowledge, as shown, for example, in the SI Sec. S13.

The most likely values of γ and q, given the data, are the ones minimizing the residuals of the NMF. The model can be expanded to several FRET components with different rates, which is a typical situation in FRET due to the variation in the distance and the relative orientation of the donor and acceptor transition dipoles (Gopich and Szabo, 2012). Such a variation can be efficiently rationalized using a distribution of rates $P(\gamma; \bar{\gamma}, \sigma)$ of mean value $\bar{\gamma}$ and relative standard deviation σ, resulting in the FRET dynamics

$$\mathbf{T}^{\mathrm{f}}(\bar{\gamma}, \sigma, q) = \int P(\gamma; \bar{\gamma}, \sigma)\tilde{\mathbf{T}}^{\mathrm{f}}(\gamma, q)d\gamma\,. \tag{12}$$

Again, the most likely values of the parameters $\bar{\gamma}$, σ, and q minimize the residual of the NMF, which are found using a computationally efficient method detailed in the SI Sec. S7.

In the following, we consider a log-normal distribution (Balakrishnan et al., 1994) of rates with mean $\bar{\gamma}$ and standard deviation $\bar{\gamma}\sigma$, which can be written as

$$P_{\ln}(\gamma) = \frac{1}{\gamma\zeta\sqrt{2\pi}}\exp\left(-\frac{1}{8}\left(\frac{2}{\zeta}\ln\left(\frac{\gamma}{\bar{\gamma}}\right) + \zeta\right)^2\right), \tag{13}$$

where $\zeta = \sqrt{\ln\left(\sigma^2 + 1\right)}$. Interestingly, this distribution can also determine the mean and standard deviation of the donor–acceptor distance. In the dipole approximation, and for a given relative donor and acceptor orientation or fast orientational averaging, the FRET rate is simply expressed as $\gamma = \gamma_{\mathrm{D}}(R_0/R)^6$, with the Förster radius R_0, the free donor decay rate γ_{D}, and the donor–acceptor distance R. Using this expression, the extracted log-normal distribution in the FRET rate γ of mean $\bar{\gamma}$ and standard deviation $\sigma\bar{\gamma}$ can be analytically expressed by a log-normal distribution in distance given by

$$P(R) = \frac{6}{R\zeta\sqrt{2\pi}} \times \exp\left(-\frac{1}{8}\left(\frac{2}{\zeta}\left(\ln\left(\frac{\gamma_{\mathrm{D}}}{\bar{\gamma}}\right) + 6\ln\left(\frac{R_0}{R}\right)\right) + \zeta\right)^2\right). \tag{14}$$

The first and second moments of this distribution can be calculated as

$$\bar{R} = \int_0^{\infty} R\,P(R)dR = R_0\sqrt[6]{\frac{\gamma_{\mathrm{D}}}{\bar{\gamma}}}\left(\sigma^2 + 1\right)^{\frac{7}{72}} \tag{15}$$

and

$$\overline{R^2} = \int_0^{\infty} R^2\,P(R)dR = R_0^2\sqrt[3]{\frac{\gamma_{\mathrm{D}}}{\bar{\gamma}}}\left(\sigma^2 + 1\right)^{\frac{2}{9}}\,, \tag{16}$$

so that the standard deviation σ_R in distance can be determined using $\sigma_R^2 = \overline{R^2} - \bar{R}^2$ as

$$\sigma_R = R_0\sqrt[6]{\frac{\gamma_{\mathrm{D}}}{\bar{\gamma}}}\sqrt{\left(\sigma^2 + 1\right)^{\frac{2}{9}} - \left(\sigma^2 + 1\right)^{\frac{7}{36}}}. \tag{17}$$

The mean $\bar{R}$ and the standard deviation σ_R of the donor–acceptor distance is therefore obtained analytically by the parameters of the log-normal rate distribution determined by uFLIM-FRET.

3. Results and discussion

3.1. uFLIM application I: Single spectral channel datasets

Here, we demonstrate the uFLIM analysis of experimental data reported in Chennell et al. (2016), in which the fluorescence lifetime of a dye changes due to variations in the environmental conditions, specifically the T2-AMPKAR construct in the presence of the 991 activator resulting in FRET. In these measurements, a single channel detects the dynamics of the T2-AMPKAR compound using time-correlated single photon counting (TCSPC) with 50 ps time bins. We have analysed the data in Fig. 4 of Chennell et al. (2016), with 4 × 4 spatial binning and a temporal binning as discussed in S1, using $t_{\mathrm{b}} = 100\,\mathrm{ps}$ and $r_{\mathrm{b}} = 0.1$. Data have been factorized by uFLIM into two components using a whitening threshold $\xi = 1$, as shown in Fig. 2 for a selection of activator concentrations (complete results are shown in the SI Fig. S1). We have measured a computational time of about 0.6 μs/pixel for a single uFLIM step on an Intel i7-8700 CPU. We found that convergence (error change below 1‰ per iteration) was reached within about 10 iterations. Further computational times reported below refer to the same CPU.

The dynamics $\mathbf{T}_{1,2}$ of the components (see Fig. 2 bottom) suggest that the first component, showing a slower decay, represents the emission of T2-AMPKAR without 991, while the second represents the T2-AMPKAR - 991 pair. For visualization, the spatial distributions $\mathbf{S}_{1,2}$ are encoded using a hue-saturation-value (HSV) colour mapping at maximum saturation. The value (V), which is the brightness, is taken as the square root of $\mathbf{S}_1 + \mathbf{S}_2$, normalized for each image. The hue (H) is given by the point-wise contrast $(\mathbf{S}_2 - \mathbf{S}_1)/(\mathbf{S}_1 + \mathbf{S}_2)$, offset and scaled as indicated. We observe a change of colour of the HSV maps from green to violet with an increasing concentration of 991, showing an increasing fraction of T2-AMPKAR with 991 attached. To compare with the global fitting exponential decay analysis in Chennell et al. (2016), the average lifetime $\langle\tau\rangle = (\{\mathbf{S}_1\}\tau_1 + \{\mathbf{S}_2\}\tau_2)/(\{\mathbf{S}_1\} + \{\mathbf{S}_2\})$ is given in the inset of the bottom panel in Fig. 2, where τ_2 and τ_3 are the lifetimes of the individual components given by the first moments of their dynamics. The resulting $\langle\tau\rangle$ exhibits a dependence on the activator concentration consistent with Chennell et al. (2016). The applied spatial and temporal binning increases the average number of photons per point well above one, from 0.19 in the original data to 17 in the binned data, improving the outcome of the factorization, as we detail in the SI Sec. S2.

This example shows that uFLIM is able to analyse FLIM experiments with the resulting weighted average lifetime showing a similar dependence as the value obtained by the global exponential fitting, yet providing the dynamics of the components not constrained to an exponential decay. As an additional example, we show in the SI Sec. S3 the uFLIM analysis of time-gated FLIM images of mixtures of two different dyes, and its ability to recover their dynamics and distribution.

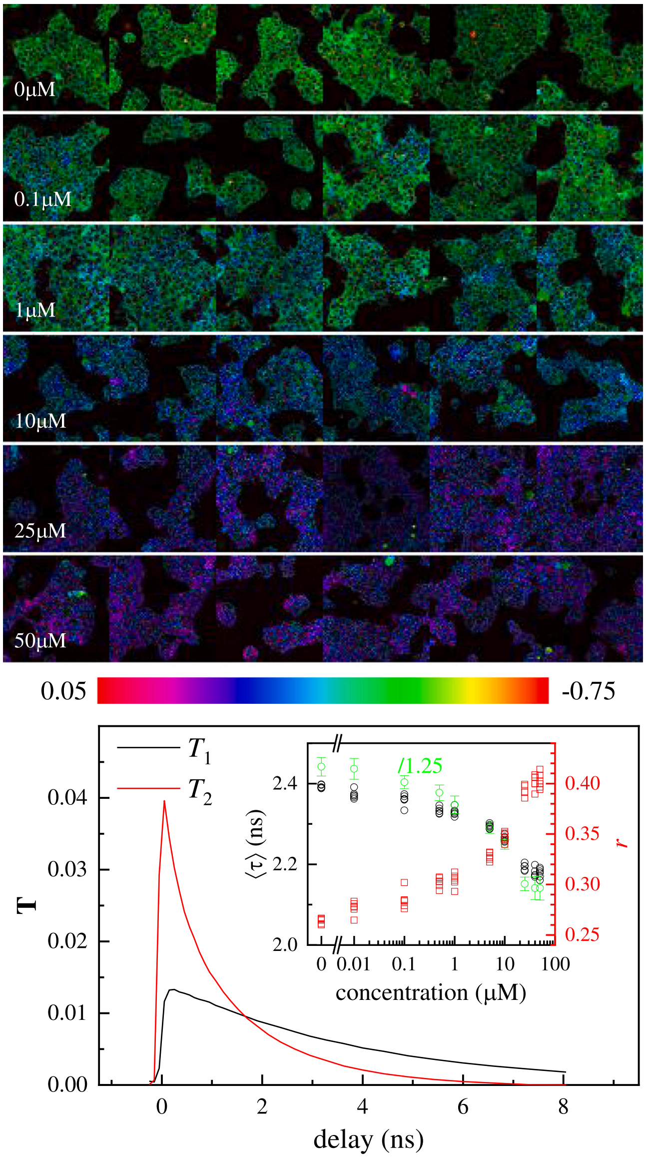

Fig. 2. Results of the uFLIM algorithm applied on a dataset from Chennell et al. (2016) of TCSPC FLIM on HepG2 expressing the T2-AMPKAR compound as a function of the concentration of the 991 activator. In these measurements, a single channel detects the dynamics of the T2-AMPKAR compound. The data have been factorized into two components which show different dynamics. Top: Concentrations $\mathbf{S}_1$ and $\mathbf{S}_2$ displayed with an HSV mapping as discussed in the text for different concentrations of 991 as indicated. The contrast is encoded as the hue of the colour. Bottom: Temporal dynamics $\mathbf{T}$ of the two retrieved components. Inset: Weighted average lifetime $\langle\tau\rangle$ (black symbols) and fraction of $\mathbf{S}_2$ in each image $r = \{\mathbf{S}_2\}/(\{\mathbf{S}_1\}+\{\mathbf{S}_2\})$ (red symbols) for the different fields of view versus the activator concentration. The green symbols show the lifetime estimated in Chennell et al. (2016), obtained by global least square fitting, divided by 1.25.

3.2. uFLIM application II: Multiple spectral channels and unmixing of many fluorescent proteins

Imaging living cells which are expressing multiple fluorescent proteins (FPs) is crucial when disentangling the protein interaction network. Here, we explore the capability of uFLIM to extract the spatial distribution of a large number of FPs, by unmixing their spectral and temporal profiles. A similar question was asked in Niehörster et al. (2016) using a pattern-matching algorithm on spectrally-resolved fluorescence lifetime imaging microscopy (sFLIM) data. sFLIM was employed with sequential excitation at three wavelengths and detection over 32 spectral channels. Up to nine fluorescent probes could be separated, for data having a photon budget of around 1000 photons per pixel in the bright regions. However, this result required prior knowledge of fluorescence decay and spectral signature patterns, a constrain that can be lifted with uFLIM.

To test the performance of uFLIM on sFLIM datasets, we generated synthetic data combining several FPs. Since the large number of excitation and detection channels used in Niehörster et al. (2016) are not available in most FLIM experimental set-ups, we simulate here a much simpler system with only two excitation lasers (at wavelengths of 460 nm and 490 nm) and two detection channels (over wavelength ranges of 500–550 nm and 550–700 nm). We use an excitation repetition rate of $r = 40\,\mathrm{MHz}$, a detection range from −1 ns to 24 ns with $l = 1000$ temporal channels, and a Gaussian instrument response function $\exp(-t^2/w^2)$ with $w = 141.4\,\mathrm{ps}$.

We first consider eight known FPs numbered by the index f (see SI Table S1), with spatial distributions given by selected paintings (Wikipedia), which were cropped and resized to 256 × 256 pixels, converted to greyscale using a gamma of 1.5 and normalized to have unity mean, yielding the distribution matrix $\mathbf{F}_f$. For each combination of excitation wavelength (index e) and detection channel (index d), we define a scaled spatial distribution $\mathbf{F}_{def} = c_{def}\mathbf{F}_f$, where c_{def} accounts for the quantum efficiency and the extinction coefficient of the FP, and the fraction of photon emission by FP f detected by channel d, see SI. We also define the fraction of photons detected in a given channel as $\hat{c}_{def} = c_{def}/\sum_{d,e} c_{def}$, and the fraction of detected photons contributed by a given FP as $\hat{c}_f = \sum_{d,e} c_{def}/\sum_{d,e,f} c_{def}$. The measured FP dynamics over the time t, represented by the matrix $\mathbf{T}_f$, are calculated as the convolution between the Gaussian IRF and a mono-exponential decay with a decay rate γ_f given by the inverse lifetime τ, see SI Sec. S5i. The noiseless sFLIM synthetic data are then obtained by multiplying the paintings with the FP dynamics, and summing the resulting FP emission, assuming equal spatially-integrated numbers of each FP, yielding

$$\mathbf{D}^{\mathrm{s}}_{ed} = A \sum_f \mathbf{F}_{def}\mathbf{T}_f \,, \tag{18}$$

where the normalization A is ensuring $\{\mathbf{D}^{\mathrm{s}}\} = N_{\mathrm{s}} I^{\mathrm{t}}$, and the average number of photons I^{t} per spatial point was chosen to be 100 or 10^4 in the results shown. To simulate photon counting detection and corresponding noise, the integer values of a random variable following Poisson statistics with a mean value given by the noiseless sFLIM data are taken as sFLIM data. Computational time was reduced by partially binning the 1000 time channels in $\mathbf{T}_f$ according to the method described in the SI Sec. S1, using $r_{\mathrm{b}} = 0.05$ and $t_{\mathrm{b}} = 25\,\mathrm{ps}$.

This synthetic data is then analysed by uFLIM according to the method described in Section 2.1 with $\xi = 0$ whitening threshold for the spatial and time averages. As a first test, for direct comparison with Niehörster et al. (2016), we retrieved the spatial distribution $\mathbf{S}^{\mathrm{w}}$ in a single step NMF, with the dynamics $\mathbf{T}^{\mathrm{w}}$ fixed by $\mathbf{T}_f$, i.e. assuming prior knowledge on the dynamics. The resulting $\mathbf{S}$ are shown in Fig. 3 for $I^{\mathrm{t}} = 10^4$. To quantify the retrieval performance, we calculated the root-mean-squares (rms) r of the distribution differences $\mathbf{S}_f - \hat{c}_f I^{\mathrm{t}}\mathbf{F}_f$ for each FP f and the corresponding relative error Π obtained by dividing r by the rms of $\hat{c}_f I^{\mathrm{t}}\mathbf{F}_f$. The spatial distributions of all eight FPs are well retrieved, with r of a few hundred photons, comparable to the shot noise, and Π of 5 to 40%. We emphasize that this was achieved using only two channels in excitation and detection, compared to 3 and 32 channels in Niehörster et al. (2016). FPs with properties differing significantly from each other are well recovered, while more error is visible for FPs with similar properties, for example, for mEos2 and mVenus, and for FPs with weak emission, such as LSS-mKate2. Even for a much smaller photon budget $I^{\mathrm{t}} = 100$ (see SI Fig. S7), spatial distributions are recovered, albeit with accordingly larger noise and reconstruction error.

To evaluate if the retrieval could be improved by an accurate treatement of the Poisson noise, we have implemented a gradient descent

Fig. 3. Spatial distributions obtained by applying uFLIM to sFLIM synthetic data generated with 8 FPs (see labels), having spatial patterns given by selected paintings, and detected by a two-channel FLIM set-up (see text). uFLIM, in this case, assumes prior knowledge on the FP dynamics, i.e. uses fixed $\mathbf{T}_f$. Greyscale is from m to M. Top rows: Retrieved $\mathbf{S}$with $m = 0$ and the maximum (M) as indicated. The spatially averaged pixel values (a) are also given, for comparison with the nominal values $\hat{c}_f I^t$, see Table S1. Bottom rows: Difference between the nominal and retrieved distributions corresponding to the top rows, with M and m as given.

Table 1
Spectral properties and lifetimes of the 5 FPs used in the synthetic sFLIM data analysed in Fig. 4. The values retrieved from a single data realization by uFLIM for $I^t = 10^4$ are given in red, where the lifetimes are the first moment of the retrieved dynamics for positive times. The standard deviations of the retrieved parameters due to photon shot noise are given in green.

Name of FP/ *painting*	f	$\hat{c}_{11f}$	$\hat{c}_{12f}$	$\hat{c}_{21f}$	$\hat{c}_{22f}$	$\hat{c}_f$	τ (ns)
WasCFP/ *The creation of Adam*	1	0.27 0.28 2.2e−4	0.07 0.08 1.4e−4	0.53 0.51 2.8e−4	0.13 0.13 1.2e−4	0.36 0.41 3.0e−4	5.05 4.73 0.017
BrUSLEE/ *The Hay Wain*	2	0.26 0.26 1.3e−4	0.09 0.07 1.6e−4	0.52 0.53 1.6e−4	0.14 0.14 0.9e−4	0.22 0.20 1.6e−4	0.94 0.95 4.8e−4
mBeRFP/ *The ambassadors*	3	0.01 0.01 1.4e−4	0.64 0.65 2.9e−4	0.01 0.01 2.9e−4	0.34 0.33 3.8e−4	0.19 0.19 2.1e−4	2.31 2.24 0.0024
Dendra2(Red)/ *Old woman and boy with candles*	4	0.01 0.01 3.8e−4	0.44 0.44 2.4e−4	0.01 0.01 4.0e−4	0.54 0.54 3.0e−4	0.13 0.13 2.8e−3	4.46 4.38 0.0024
MiCy/ *The great wave off Kanagawa*	5	0.63 0.80 6.4e−4	0.11 0.12 6.2e−4	0.22 0.08 7.8e−4	0.04 0.00 2.8e−4	0.10 0.07 1.3e−4	3.90 3.72 0.0027

minimizing the KLD. We have used a multiplicative update rule (Lee and Seung, 2001), and, as an initial guess of $\mathbf{S}$, either the solution of the linear system $\mathbf{D} = \mathbf{ST}$ (see SI Sec. S4), or the result of the NMF. In both cases, we did not observe a relevant improvement of the results compared to the fast NMF algorithm (see SI Fig. S8 and Fig. S9 for $I^t = 10^4$ and Fig. S10 and Fig. S11 for $I^t = 100$), despite a 15–50 times longer computational time. Using the fast NMF, the uFLIM computational time was 5 μs/pixel. This indicates that the whitening transformation, combined with fast NMF algorithm, is a suitable alternative to the computationally expensive gradient descent method.

Next, we applied uFLIM to retrieve the spatial distribution and the FP spectral and dynamic properties directly from the simulated photon counting data, with no prior knowledge. Since determining the FP properties additionally to the spatial distribution is more taxing on the data information content, we have removed the three FPs with the smallest differences in their properties from the eight previously used (see Table 1). To introduce unknown variations from the nominal FP properties, often encountered in the cellular environment, the sFLIM data are generated with a ±20% relative variation in c_{def} and $1/\gamma_f$, and an additional ±5% on the resulting $\hat{c}_f$, taken at random from a uniform distribution. We use the iterative uFLIM method, where both $\mathbf{S}$ and $\mathbf{T}$ are calculated. The nominal FP properties, before parameter variation, are used to generate the initial value of $\mathbf{T}$, while the guesses for $\mathbf{S}$ are obtained by solving the system $\mathbf{D} = \mathbf{ST}$ and then setting negative values to zero. We constrain the dynamics of a given FP to be the same for all excitation and detection channels by replacing at each NMF iteration step the dynamics calculated for the different channels with their average. The iteration is stopped if the factorization error has not improved for three consecutive steps, allowing for a maximum of 100 iterations. Here, a single iteration step took about 2 μs/pixel, and typically 10–25 steps were used.

Fig. 4 shows the retrieved spatial distributions and FP properties obtained for $I^t = 10^4$. The spectral and temporal properties extracted from the retrieved quantities are given in red in Table 1, showing a good agreement between the retrieved and original $\mathbf{S}$ and $\mathbf{T}$, with $\mathbf{T}$ being slightly faster. Even for $I^t = 10^2$ (see SI Fig. S13), the retrieval works reasonably, showing only some cross-talk between the FPs with most similar properties, mBeRFP and Dendra2(Red). Results can be slightly improved by subsequently minimizing the KLD (see SI Fig. S18 and Fig. S19). However, this takes two to five times longer than the fast NMF, depending on I^t and the choice of initial guesses.

We note that the number of FPs retrievable within a certain error depends in a complex way on their properties, especially on their differences, as well as the signal strength I^t, and the FP spatial distributions. Therefore, for a given experiment, a reliable determination of the retrieval error should be obtained via repeated retrievals using new realizations of the photon counts $\mathbf{D}$ from probability distributions determined by the measured counts. To give an example, for the parameters shown in Table 1, we evaluated ten realizations of the photon shot noise, and found that the absolute deviations for $\hat{c}_{def}$ and $\hat{c}_f$ and the relative deviation for τ are below 1%, as shown in Table 1.

To exemplify the benefits of using retrieved properties versus fixed properties, we show in the SI Fig. S21 the FP distributions obtained from the data of Fig. 4 fixing the FP properties to the nominal ones, not including the variations introduced. Significant systematic errors are found for weak FPs, e.g. Dendra2(Red) and MiCy. With decreasing I^t, the noise in the data is increasing and the relative importance of the systematic error decreases, so that for $I^t = 100$ (see SI Fig. S22), they are less relevant.

We emphasize that while we have chosen here exponential dynamics allowing to use known FP parameters, the method is applicable for any dynamics – as example we show in the SI Sec. S5v results for a log-normal distribution. The retrieval quality, even when using a broad distribution $\sigma = 0.8$, is similar to the case of exponential dynamics, confirming that the method is suited for a wide range of FP dynamics.

We stress that retrieving both the spatial distribution and the FP spectral and dynamic properties from the measured data eliminates the need for separate measurements on reference samples with individual FPs. Notably, the spectral and dynamic properties of FPs vary with their environment, and thus can be different between pure solutions and cellular samples. Furthermore, a long-term drift of the instrument response can introduce systematic deviations between the FP properties used and the ones present in the sample of interest. Removing the need for such prior knowledge is, therefore, a major advantage of uFLIM.

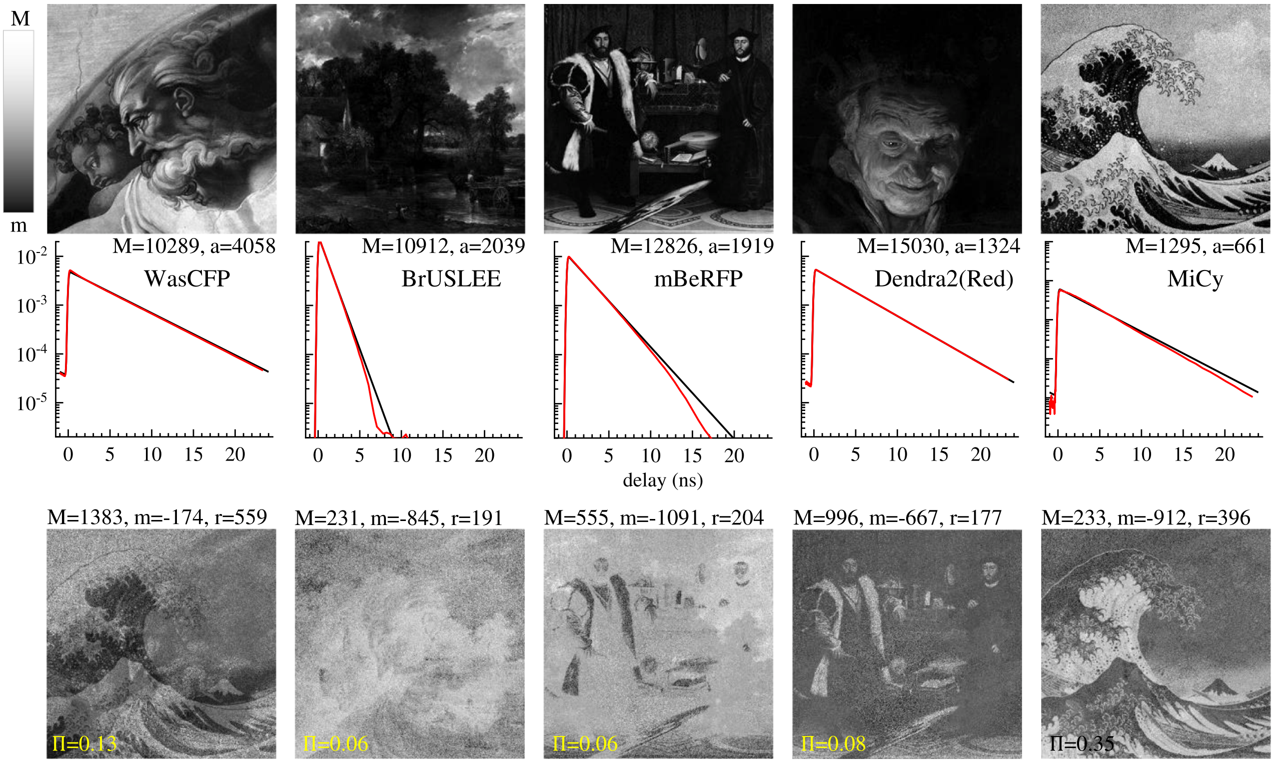

Fig. 4. Spatial distributions and properties of 5 FPs retrieved by uFLIM from sFLIM synthetic data with $I^t = 10^4$, generated as described in the text, on a greyscale from m to M. Here, uFLIM is applied with no prior knowledge on the FP properties. Top row: Retrieved $\mathbf{S}$ with $m = 0$ and the maximum M as indicated. The spatially averaged pixel values a are given, having the nominal values $\hat{c}_f I^t$, see Table 1. Middle row: Retrieved dynamics $\mathbf{T}_f$ (red), and corresponding original dynamics (black). Bottom row: Difference between the retrieved and original distributions, using M and m as given.

3.3. uFLIM-FRET application I: Analysis of synthetic data

To verify the uFLIM-FRET method, we first use synthetic data. We consider two detectors which are mostly detecting the donor and acceptor emission, respectively, given by $R^d = R^a = 0.9$. The FLIM system is the same as in Section 3.2. We consider that the donor and the acceptor fluorescence have exponential dynamics, with decay rates of γ_D= 0.33/ns and γ_A= 0.385/ns, respectively, corresponding to the decay lifetimes of mNeonGreen and mRuby. We vary the spatially averaged time-integrated photon counts of the donor emission I^d, proportional to the one of the acceptor emission, I^a, using $I^a = 0.8 I^d$ throughout. The dynamics of the DAP detected by the two channels are calculated according to Eq. (12), considering a log-normal distribution of FRET rates.

We generated data with $\bar{\gamma}$ taking values of $\bar{\gamma}_s = 0.1$/ns, 0.5/ns and 0.9/ns, and σ given by $\sigma_s = 0.5$. The relative detection efficiency between donor and acceptor was taken to be $q_s = 1$. In the following, symbols without subscript refer to the parameter values changed by the algorithm, while symbols with the subscript s refer to the values used to generate the data, and symbols with the subscript r are values resulting from the algorithm.

Various relative strengths of DAP and donor emission, I^f/I^d, are considered, where I^f are the spatially averaged time-integrated photon counts of the DAP emission. As spatial distributions of donor, acceptor, and DAP, we used Monet's *Nymphéas*, Van Gogh's *Starry Night*, and Leonardo's *La Gioconda*, respectively. The drawings (Wikipedia) were cropped, resized to 256 × 256 pixels, and converted to greyscale. The synthetic data $\mathbf{D}^s = \mathbf{S}^s\mathbf{T}^s + b$ are then created by multiplying each pixel of the images with the corresponding decay curve and adding the dark counts b, which we characterize by their equivalent intensity $I^b = bN_t$. For the data shown, we have considered $b = 0$, 0.001, and 0.01, corresponding to $I^b = 0$, 2, and 20.

The photon counting data $\mathbf{D}$ is generated from $\mathbf{D}^s$ using Poissonian statistics as before, and we repeated the analysis for 10 realizations of $\mathbf{D}$. To reduce the analysis time, we apply a time binning with t_b= 25 ps and r_b= 0.05 (see SI Sec. S1). The data are then factorized using the donor ($\mathbf{T}^d$), acceptor ($\mathbf{T}^a$), and FRET ($\mathbf{T}^f$) components over a grid of the FRET parameters $\bar{\gamma}$, σ, and q. Donor and acceptor dynamics without FRET are taken as known — in experiments, these would have been measured and retrieved by uFLIM. No free components are used so that the factorization is a single step NMF for the spatial distributions $\mathbf{S}^w$, which minimize the residual E. The initial guesses for $\mathbf{S}^w$ are random.

The dependence of the factorization error E over the parameter space is shown in Fig. 5. The top panel of Fig. 5 shows E over the coarse grid of FRET parameters $\bar{\gamma}$ and σ for $q = 1$, and $I^d = I^f = 10^4$. The bottom image shows E calculated during the grid refinement step, within the finer grid range indicated by the grey rectangle in the top panel. The residual is minimized to a relative change better than 10^{-5}. Note that the non-zero residual is due to the shot noise in the photon counts. The estimated parameter values are close to the ground truth of the simulated data (the relative errors are 0.07%, −0.72%, and 0.17% for $\bar{\gamma}$, σ and q, respectively), with remaining deviations due to the photon shot noise.

Fig. 6 shows uFLIM-FRET results for the values of $\bar{\gamma}_r$, σ_r, and q_r minimizing the residual, for a specific data realization with $\bar{\gamma}_s = 0.5$/ns, $I^b = 2$ and $\kappa = 1$. Results for small intensity and strong FRET ($I^d = I^f = 100$) are given on the left, for large intensity and weak FRET ($I^d = 16 I^f = 10000$) in the middle, and for large intensity and strong FRET ($I^d = I^f = 10000$) on the right. The first row shows the data summed over the temporal channels, $N_t\bar{\mathbf{S}}$, where the images of donor and acceptor are visible, and the FRET image is discernible for strong FRET. The synthetic data dynamics $\mathbf{T}^{s,d}$, $\mathbf{T}^{s,a}$, and $\mathbf{T}^{s,f}$, are given as solid lines in Fig. 6 (bottom). The second, third and fourth rows from the top show the spatial distributions $\mathbf{S}^d$, $\mathbf{S}^a$, $\mathbf{S}^f$ retrieved by NMF, recovering the corresponding images well, also in conditions of small intensity (left) and weak FRET (middle). The difference between the original and retrieved data is quantified using

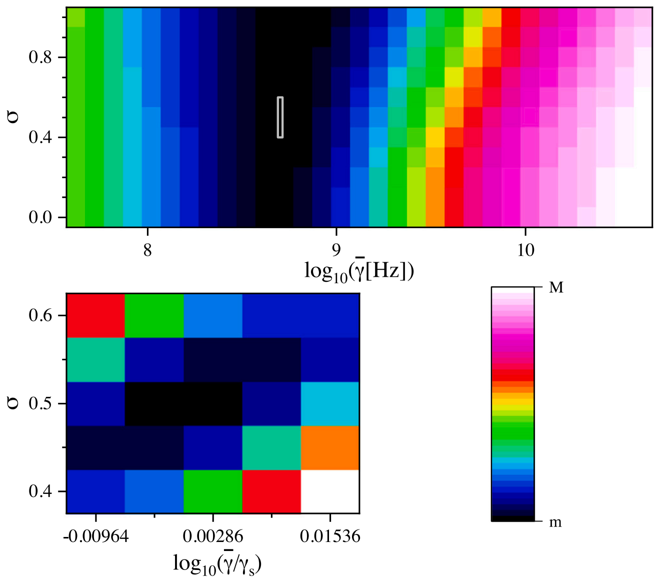

Fig. 5. Factorization error E as a function of the FRET distribution parameters $\bar{\gamma}$ and σ for $q = 1$ for data generated using $I^{\mathrm{d}} = I^{\mathrm{f}} = 10^4$, $\bar{\gamma}_{\mathrm{s}}$= 0.5/ns, σ_{s}= 0.5, q_{s}= 1, $\kappa = 1$ and $I^{\mathrm{b}} = 2$. Top: Coarse grid, $m = 399$, $M = 537$. Bottom: refined grid (see SI Sec. S7), $m = 399.163$, $M = 399.256$. The refinement domain is defined by the grey rectangle in the top panel. Colour scale as given from m to M.

the relative error $\epsilon = \|\mathbf{D}^{\mathrm{s}}-\mathbf{ST}\|_2/\|\mathbf{D}^{\mathrm{s}}\|_2$, and similarly the reconstruction of the individual components is quantified by the relative errors $\epsilon_i = \|\mathbf{S}^{\mathrm{s},i}\mathbf{T}^{\mathrm{s},i} - \mathbf{S}^i\mathbf{T}^i\|_2/\|\mathbf{S}^{\mathrm{s},i}\mathbf{T}^{\mathrm{s},i}\|_2$, where $i \in \{\mathrm{d},\mathrm{a},\mathrm{f}\}$. The mean values ($\langle.\rangle$) and the standard deviations (].[) of the reconstruction errors calculated over the data realizations are shown in the SI Fig. S34. As expected, the reconstruction error decreases with increasing intensities. We find that the error scales approximately as $1/\sqrt{I^{\mathrm{d}}}$ (see SI Fig. S35). In general, ϵ, ϵ_{d}, and ϵ_{a} depend mostly on I^{d}, while ϵ_{f} is affected by both I^{d} and I^{f}. We note that all errors are below 10% for the high-intensity case, and that they are always much larger than the parameter retrieval error, since they are dominated by the shot noise in the realizations.

The uFLIM-FRET analysis is largely superior to the phasor analysis approach, as we show in the SI Sec. S8 using the same data. Specifically, to extract quantitative information, a phasor analysis needs to assume a simple model of the dynamics, and the abundance of the donor–acceptor pairs undergoing FRET and the FRET efficiency are typically not separated. Furthermore, the spatial distributions of the donor-only and DAPs obtained with the phasor analysis poorly reflect the original distributions (see SI Fig. S30).

The uFLIM-FRET retrieved dynamics of the FRET component $\mathbf{T}^{\mathrm{f}}$ (dashed lines in Fig. 6) agree well with the ground truth, which is confirmed by the close match of true and retrieved values of the parameters $\bar{\gamma}_{\mathrm{r}}$, σ_{r}, and q_{r} given in the caption. Their mean values and standard deviations over the ensemble of realizations are given in the SI Fig. S46. The errors decrease as the intensities increase, showing that the method is correctly retrieving the FRET parameters. The standard deviation, which is due to the photon shot noise in each realization, is rather similar for the different parameters, with σ being retrieved with less accuracy as its influence on the dynamics $\mathbf{T}^{\mathrm{f}}$ is lower. However, we also see some systematics for low intensities, in particular σ is underestimated. To verify if this could be due to the remaining non-whiteness of the noise in the analysed data $\mathbf{D}^{\mathrm{w}}$, we repeated the factorization using the gradient descent minimizing the KLD, with the fast NMF results as initial guesses. The retrieved spatial distributions and FRET parameters obtained with the two methods are generally very similar (see SI Fig. S80), confirming the suitability of the fast NMF algorithm on partially whitened data for the analysis of data showing Poisson noise. Additionally, the gradient descent comes with more than two orders of magnitude longer computational time, here about 1 ms/pixel for a single CPU core for given FRET parameters, and since of the order of 5000 evaluations are used to find the parameters that minimize the error, it is unsuitable for real-time analysis.

The difference in the accuracy among the different parameters can be understood by looking at the curvature of the reconstruction error along the directions defined by the parameters. The curvature is much smaller along the σ direction, resulting in a lower accuracy in the determination of this parameter (see SI Sec. S12).

Further results for different $\bar{\gamma}_{\mathrm{s}}$ and I^{b} are given in the SI Sec. S11. In the case of a small FRET rate $\bar{\gamma}_{\mathrm{s}} = 0.1$/ns, donor and DAP dynamics are similar, making the retrieval more challenging, so that for small intensities, the FRET image bleeds through to the $\mathbf{S}^{\mathrm{d}}$ component, $\mathbf{T}^{\mathrm{f}}$ differs from $\mathbf{T}^{\mathrm{s,f}}$, and the value of σ is underestimated. For a higher rate $\bar{\gamma}_{\mathrm{s}} = 0.9$/ns instead, the DAP dynamics and spatial distribution are recovered with higher accuracy. The obtained average parameters for the two cases of $\bar{\gamma} = 0.1$/ns and $\bar{\gamma} = 0.9$/ns are also given in the SI Sec. S11. The dark count rate adds uncertainty to the retrieval. Without dark rate ($I^{\mathrm{b}} = 0$), the method is able to retrieve the correct parameters of the FRET distribution with smaller error than for $I^{\mathrm{b}} = 2$ (see SI Fig. S44 and Fig. S45), and the retrieval is possible for intensities as small as $I^{\mathrm{d}} = 32$ and mean FRET rates of 0.5 and 0.9/ns. Conversely, for large dark rate ($I^{\mathrm{b}} = 20$), higher I^{d} and I^{f} are required for retrieval, see SI Fig. S47 and Fig. S48.

The dependence of the reconstruction and FRET parameter retrieval errors on the image size is analysed in the SI Fig. S37. The systematic errors of the mean FRET parameters are not significantly affected by the number of pixels N_{s}. The standard deviation, instead, scales as $1/N_{\mathrm{s}}$, which is steeper than the $1/\sqrt{N_{\mathrm{s}}}$ dependence expected for the shot noise. We note that each pixel comes with its own concentration in $\mathbf{S}$, so that the number of photons per retrieved information is independent of N_{s}, as long as the number of spatial points is much larger than the number of FRET parameters.

We have repeated the analysis in the case of negligible direct excitation of the acceptor molecules, choosing $\kappa = 0$ in Eq. (9). Accordingly, we do not include a pure acceptor component with dynamics $\mathbf{T}^{\mathrm{a}}$ in the NMF. The corresponding increase in contrast and reduction in free parameters results in smaller errors of both reconstruction and retrieved parameters, as shown in the SI Fig. S54 to Fig. S70. We also show the ability of uFLIM-FRET to retrieve the FRET parameters and the DAP spatial distribution in the presence of an additional component, such as autofluorescence, in the SI Sec. S13. The method performs well even in the presence of multiple autofluorescent species, such as bound and unbound NADH and FAD, when taking data for additional excitation and detection channels, as shown in the SI Sec. S14.

We have also considered the case of environmental conditions which could alter the dynamics, such as a spatial dependent pH, resulting in a modification of the unquenched donor dynamics similar to a FRET process. By providing two donor and two acceptor dynamics, corresponding to the end points of the pH dependence present in the data (such dynamics could be extracted from uFLIM analysis), and including a constrain given by a single spatially dependent environmental parameter, we show in the SI Sec. S15 that such environment effects can be disentangled from the FRET process and quantified by the uFLIM-FRET method.

3.4. uFLIM-FRET application II: Analysis of experimental data

To show that uFLIM-FRET works well also with experimental data, we analysed FLIM-FRET *in vivo* experiments using the data published in Smith et al. (2019), where four Matrigel plugs containing different donor (AF700)-acceptor (AF750) ratios (ROI_1: D:A = 1:0, ROI_2: D:A = 1:1, ROI_3: D:A = 1:2, ROI_4: D:A = 1:3) are implanted subcutaneously into a mouse and imaged (Smith et al., 2019; Sinsuebphon et al., 2018). Only one channel, centred at the donor emission, has been acquired in the FLIM measurements. In the analysis, the data of the regions

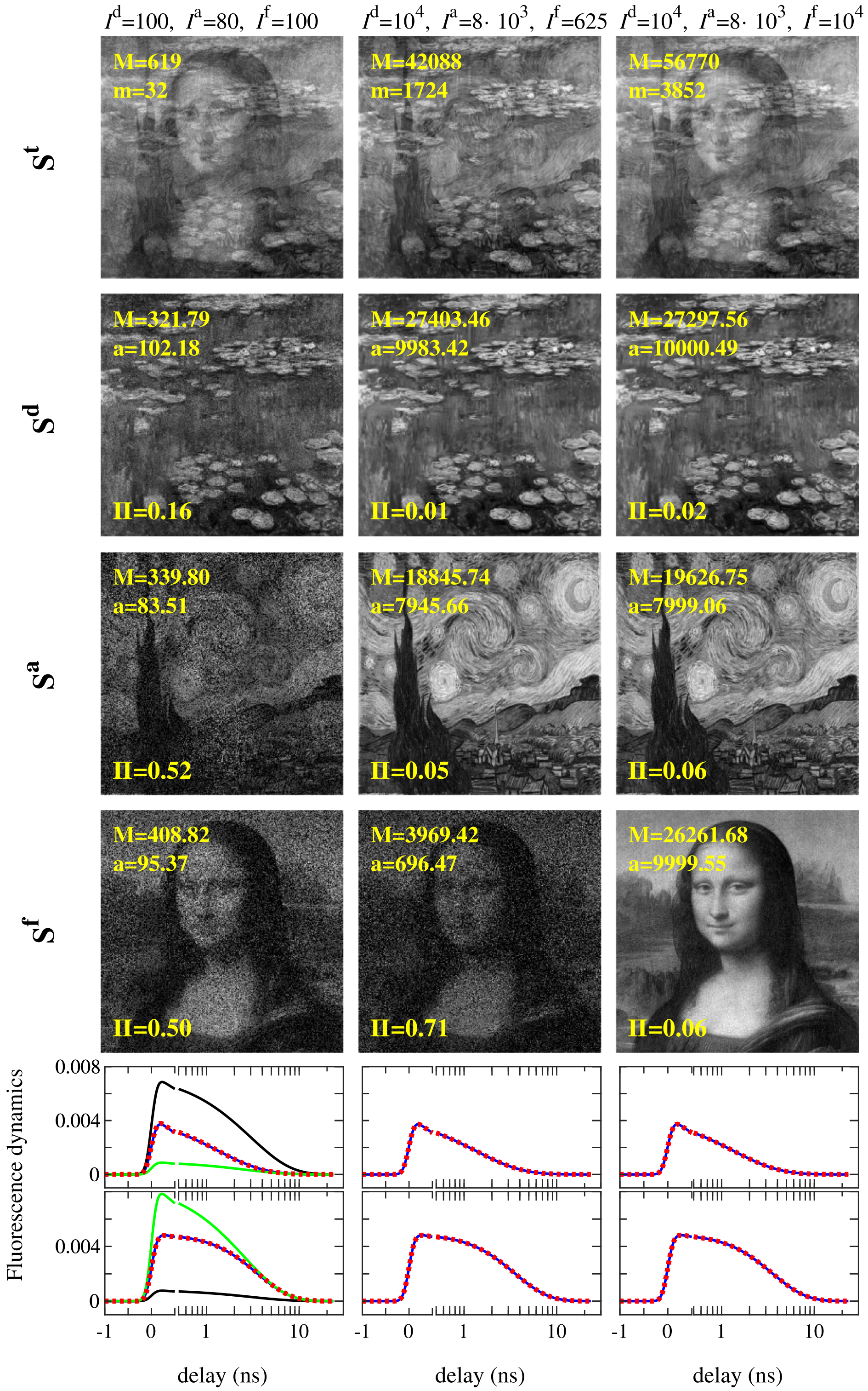

Fig. 6. Results of uFLIM-FRET for synthetic data generated using $\bar{\gamma}_s = 0.5/\text{ns}$, $\sigma_s = 0.5$, $q_s = 1$, $I^b = 2$ and $\kappa = 1$. The three columns refer to different intensities, as indicated on the top. Top row: the time summed data $\mathbf{S}^t = N_t\bar{\mathbf{S}}$, on a linear grey scale from a minimum m (black) to a maximum M (white) as indicated. The second to fourth rows show the retrieved spatial distributions of the donor $\mathbf{S}^d$, acceptor $\mathbf{S}^a$, and FRET $\mathbf{S}^f$. Here $m = 0$, and a is the average pixel value over the image. The bottom panels show the ground truth dynamics of donor $\mathbf{T}^d$ (black), acceptor $\mathbf{T}^a$ (green), and DAPs undergoing FRET $\mathbf{T}^f$ (blue), with the retrieved FRET dynamics given as red dashed lines. The signals acquired at the donor (acceptor) detector are given in the top (bottom) panel, respectively. The dynamics are normalized to have a sum of unity over the 2000 temporal points of both detectors. The retrieved FRET rate distribution parameters are $\bar{\gamma}_r = (480.52 \pm 0.03)/\mu\text{s}$, $\sigma_r = 0.0732 \pm 0.0013$ and $q_r = 0.98143 \pm 0.00007$ for the first column, $\bar{\gamma}_r = (502.55 \pm 0.39)/\mu\text{s}$, $\sigma_r = 0.5201 \pm 0.0019$ and $q_r = 0.99961 \pm 0.00006$ for the second column, and $\bar{\gamma}_r = (499.72 \pm 0.11)/\mu\text{s}$, $\sigma_r = 0.499 \pm 0.00055$, and $q_r = 1.00042 \pm 0.00002$ for the third column. The errors given are the uncertainty of the minimum position of the second order polynomial fit to the reconstruction error (see Fig. 5).

corresponding to the four Matrigel plugs were used. Before performing the uFLIM-FRET, we compensated for the possible pixel-dependent variation of the laser pulse arrival time. For each pixel, we defined the pulse arrival time as the time when the measured intensity is half of the maximum recorded signal. To align the time axis, data were interpolated, and we used linear extrapolation to take into account

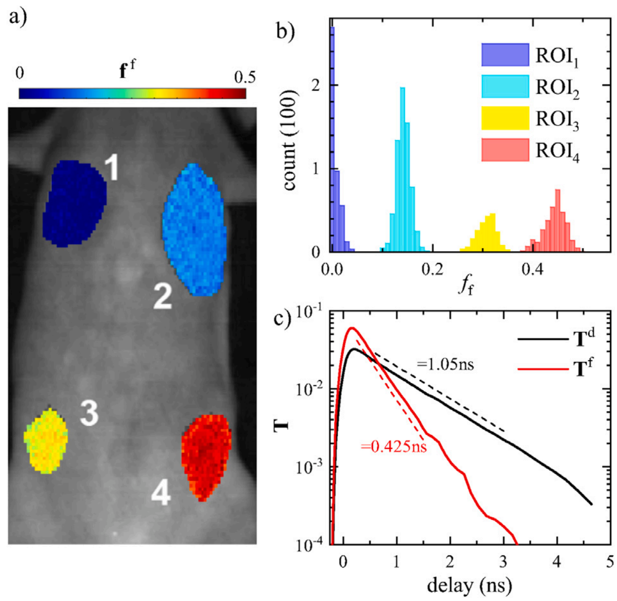

Fig. 7. Results of the uFLIM-FRET analysis on data from Smith et al. (2019). The different Matrigel plugs contain different donor–acceptor ratios (ROI$_1$: D:A = 1:0, ROI$_2$: D:A = 1:1, ROI$_3$: D:A = 1:2, ROI$_4$: D:A = 1:3). (a) Spatial distribution of the quenched donor fraction f^{f} in the different ROIs. (b) Histograms of f^{f} measured in the four ROIs. c) Dynamics of the uFLIM-FRET components for the unquenched ($\mathbf{T}^{\mathrm{d}}$, black) and quenched ($\mathbf{T}^{\mathrm{f}}$, red) donor.

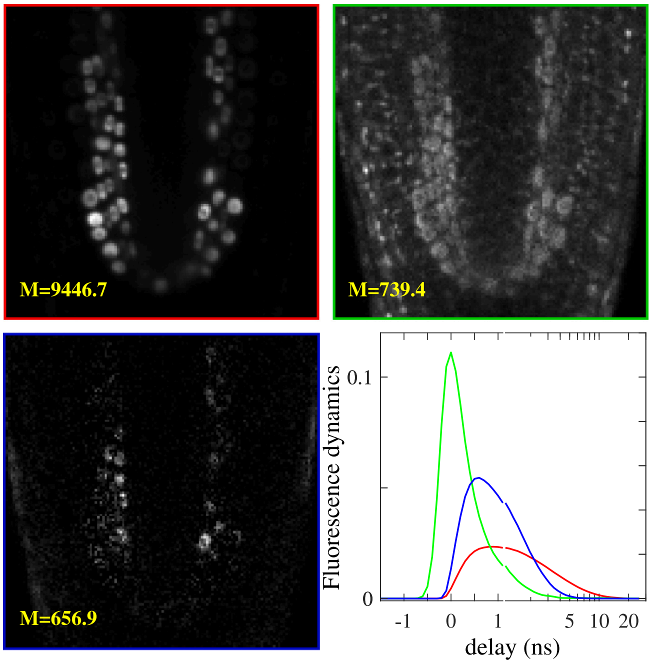

Fig. 8. uFLIM-FRET analysis of pSCR expressed SCR and SHR in the Arabidopsis root endodermis. The images show the distribution of the three components used in the uFLIM-FRET analysis on a greyscale as in Fig. 4 with m = 0. Red: donor (*pSCR::SCR:YFP*), green: autofluorescence, Blue: DAP. The corresponding dynamics $\mathbf{T}^{\mathrm{d}}$ (red), $\mathbf{T}^{\mathrm{f}}$ (blue), and $\mathbf{T}^{\mathrm{u}}$ (green) are shown in the graph.

the truncated dynamics. Only data with a delay larger than −0.22 ns were used to limit the contribution of the signal at negative time delays.

After these pre-processing steps, we have used the pixels in the Matrigel region with D:A = 1:0 (ROI$_1$) to obtain the dynamics of the free donor applying uFLIM with one component. The data were temporally binned (t_{b} = 0.04 ns and r_{b} = 0.05) to improve the single pixel signal-to-noise ratio and reduce computational time. We note that such a temporal binning step might be useful also for other analysis methodologies. uFLIM-FRET was then used to estimate the distribution of the DAP undergoing FRET, including all pixels in the four ROIs. Since the data were acquired using only a single channel resonant with the donor emission, and the acceptor bleed-through was not characterized, we have performed our analysis assuming R^{a} = 1 and κ = 0 and searching for the combination of $\bar\gamma$ and σ minimizing the NMF error. We did not apply partial whitening as the noise in the data did not show a significant intensity dependence, which may be due to dominating read noise or other classical noise.

Fig. 7 shows the results of the uFLIM-FRET analysis. The retrieved FRET rate distribution has a mean rate $\bar\gamma$ of about 1.2 GHz with a negligible width ($\sigma \sim 0$). We calculated the fraction of photons emitted by the donor undergoing FRET as point-wise $f^{\mathrm{f}} = \mathbf{S}^{\mathrm{f}}/\left(\mathbf{S}^{\mathrm{d}}+\mathbf{S}^{\mathrm{f}}\right)$. The spatial distribution of f^{f} is shown in Fig. 7a. The different ROIs present rather uniform values of f^{f} quantified by the histograms in Fig. 7b. The retrieved dynamics of the unquenched ($\mathbf{T}^{\mathrm{d}}$) and quenched ($\mathbf{T}^{\mathrm{f}}$) donor (Fig. 7c) show approximately mono-exponential decays with lifetimes of 1.05 ns and 0.425 ns, respectively. Our results are consistent with least-square fitting and deep-learning approaches (see SI of Smith et al. (2019)). Importantly, uFLIM-FRET retrieves a more uniform distribution of f^{f} in the different ROIs (narrower histograms), which is closer to the uniform distribution expected from the experiment.

Additional unknown fluorescence components, such as autofluorescence, can be included in uFLIM-FRET, as we demonstrate here using FLIM-FRET experiments reported in Long et al. (2017) on Arabidopsis roots co-expressing two tagged interacting transcription factors, SHORT-ROOT (SHR) and SCARECROW (SCR). The levels of both proteins are elevated in the endodermis controlled by the SCR promoter (pSCR). The SCR factor is tagged with YFP acting as donor, while the SHR protein is tagged with the RFP acting as acceptor. Only one channel, centred at the donor emission, has been acquired in the FLIM measurements. The data were binned both spatially (2 × 2) and temporally (t_{b} = 100 ps, r_{b} = 0). We used uFLIM on images of roots expressing only *pSCR::SCR:YFP* to retrieve the donor ($\mathbf{T}^{\mathrm{d}}$) and autofluorescence ($\mathbf{T}^{\mathrm{u}}$) dynamics. Using these dynamics, we have applied uFLIM-FRET on data from roots co-expressing *pSCR::SCR:YFP* and *pSCR::RFP:SHR*, using r_{b} = 0.1, and the time zero was set to the peak of the autofluorescence component. Since only the donor was measured, we used R^d = 1 and R^a = 0 and the FRET dynamics simplified to

$$\mathbf{T}^{\mathrm{f}}(\bar\gamma,\sigma)=\int P(\gamma;\bar\gamma,\sigma)\tilde{\mathbf{T}}^{\mathrm{d}}(\gamma)d\gamma\,. \tag{19}$$

Fig. 8 shows the results of uFLIM-FRET, yielding $\bar\gamma_{\mathrm{r}}$ = 0.57/ns and $\sigma_{\mathrm{r}} \sim 0$. This corresponds to a quenched donor decay time of $\tau_{\mathrm{f}} = \tau_{\mathrm{d}}/(1+\bar\gamma_{\mathrm{r}}\tau_{\mathrm{d}}) = 1.2$ ns and a FRET efficiency of $E = 1-(\bar\gamma_{\mathrm{r}}\tau_{\mathrm{d}}+1)^{-1} = 0.66$, where a donor lifetime of $\tau_{\mathrm{d}} = 3.57$ ns has been estimated from the first moment of $\mathbf{T}^{\mathrm{d}}$.

The analysis reveals an accumulation of DAPs in the endodermis of the root, where both donor and acceptor are expressed, in line with the reported single-pixel lifetime analysis of Long et al. (2017) (see also the distribution of the retrieved average lifetime in the SI Sec. S16). The computational time was about 2 μs/pixel for a single iteration performed by a single CPU core, and some 700 iterations were used to find the parameters that minimize the error. With our CPU, the total analysis time was about 10 s, including fitting. The computational time can be significantly reduced if a GPU is used, allowing more parallel calculations. As with the synthetic data, using the gradient descent minimizing the KLD instead of fast NMF does not lead to significant changes in the parameters ($\bar\gamma_{\mathrm{r}}$ = 0.47/ns and $\sigma_{\mathrm{r}} \sim 0$, see SI Fig. S81).

4. Conclusion

We have demonstrated a data analysis method, which we call uFLIM, to analyse FLIM data in an unsupervised way. It employs a fast non-negative factorization algorithm on partially whitened data to infer the emission dynamics and the spatial distribution of emitting molecules. The method offers several advantages compared to other approaches in the analysis of FLIM data available in the literature. Firstly, it does not make assumptions on the shape of the dynamics, which is instead the starting point of standard fitting techniques. Secondly, the algorithm does not require reference patterns, which are the component dynamics, as input. It can unmix spectrally resolved FLIM images where several spectrally overlapping fluorescing probes are present, extending the multiplexing capabilities of FLIM. Furthermore, the method uses a fast NMF algorithm, capable of analysing data in real-time on desktop computers. This speed comes with an approximate treatment of the noise in the data, but we have verified that the resulting systematic errors in the retrieval are not significant by comparing with a gradient descent algorithm that uses the exact noise model of the data, at the cost of orders of magnitude longer computational time.

Based on uFLIM, we developed uFLIM-FRET, which extracts FRET rates and spatial distributions. Here, the individual donor (and acceptor if detected) emission dynamics, which can be determined by uFLIM, are used to calculate the DAP dynamics for a distribution of FRET rates. uFLIM-FRET determines the values of the FRET distribution parameters which minimize the residual of the NMF, at the same time as determining the spatial distribution of donor, acceptor, and DAPs. The distribution parameters characterize the fluctuations in the separation and orientation of the donor and acceptor in the DAP, going beyond the approximation of a single FRET rate. Additional known or unknown components can be added to the retrieval. uFLIM-FRET can estimate the FRET parameters even in the presence of unknown autofluorescence. The method can be adapted to retrieve donor, acceptor, and DAP dynamics without separate donor and acceptor data. Generally, the more information is available, the more parameters can be retrieved. The precision of retrieval depends on the corresponding effect on the data – the larger the difference between, for example, donor, acceptor, and FRET dynamics over the detected channels, the higher the precision.

Both uFLIM and uFLIM-FRET have been demonstrated on synthetic data with known ground truth and realistic photon shot-noise, as well as on experimental data taken from a range of applications, showing its wide suitability and performance. FRET could be retrieved even in presence of spatially varying donor and acceptor lifetimes due to e.g. pH dependencies, and in the presence of strong autofluorescence with multiple components, such as bound and free FAD and NADH.

Notably, the method also offers the possibility to compress the data of FLIM experiments into the spatial distributions of few components, which facilitates the usage of FLIM-FRET as a high-throughput tool for cell biology.

In order to enable widespread adoption of uFLIM-FRET as a method of choice to analyse FLIM data, the corresponding software is provided (http://langsrv.astro.cf.ac.uk/uFLIM/uFLIM.html). Information on the data underpinning the results presented here, including how to access them, can be found in the Cardiff University data catalogue at http://doi.org/10.17035/d.2020.0115661402.

CRediT authorship contribution statement

Francesco Masia: Methodology, Software, Investigation, Formal analysis, Data curation, Visualization, Validation, Writing – original draft, Writing – review & editing, Funding acquisition. **Walter Dewitte:** Methodology, Writing – review & editing. **Paola Borri:** Methodology, Writing – review & editing, Resources, Funding acquisition. **Wolfgang Langbein:** Conceptualization, Supervision, Project administration, Methodology, Formal analysis, Writing – original draft, Writing – review & editing, Resources, Funding acquisition.

Declaration of competing interest

The authors declare that they have no known competing financial interests or personal relationships that could have appeared to influence the work reported in this paper.

Acknowledgements

This work was supported by the Cardiff University Data Innovation URI Seedcorn Fund, UK. F.M. acknowledges the Ser Cymru II programme (Case ID 80762-CU-148) which is part-funded by Cardiff University, UK and the European Regional Development Fund through the Welsh Government. P.B. acknowledges the Royal Society for her Wolfson research merit award, UK (Grant WM140077). The authors thank Christopher Dunsby (Imperial College London) and Ikram Blilou (King Abdullah University of Science and Technology) for kindly providing the experimental data used in the manuscript. Discussions with Peter Watson and Camille Blakebrough-Fairbairn are gratefully acknowledged.

Appendix A. Supplementary data

Supplementary material related to this article can be found online at https://doi.org/10.1016/j.media.2022.102579.

References

Agronskaia, A.V., Tertoolen, L., Gerritsen, H.C., 2004. Fast fluorescence lifetime imaging of calcium in living cells. J. Biomed. Opt. 9, 9–9–8. http://dx.doi.org/10.1117/1.1806472.

Balakrishnan, N., Kotz, S., Johnson, N.L., 1994. Continuous Univariate Distributions: Vol. 1. Wiley-Blackwell.

Berezin, M.Y., Achilefu, S., 2010. Fluorescence lifetime measurements and biological imaging. Chem. Rev. 110, 2641–2684. http://dx.doi.org/10.1021/cr900343z.

Brodwolf, R., Volz-Rakebrand, P., Stellmacher, J., Wolff, C., Unbehauen, M., Haag, R., Schäfer-Korting, M., Zoschke, C., Alexiev, U., 2020. Faster, sharper, more precise: Automated cluster-flim in preclinical testing directly identifies the intracellular fate of theranostics in live cells and tissue. Theranostics 10, 6322–6336. http://dx.doi.org/10.7150/thno.42581, URL: https://www.thno.org/v10p6322.htm.

Chennell, G., Willows, J.R., Warren, C.S., Carling, D., French, M.P., Dunsby, C., Sardini, A., 2016. Imaging of metabolic status in 3D cultures with an improved ampk fret biosensor for flim. Sensors 16 (E1312), http://dx.doi.org/10.3390/s16081312.

Clayton, A.H.A., Hanley, Q.S., Verveer, P.J., 2004. Graphical representation and multicomponent analysis of single-frequency fluorescence lifetime imaging microscopy data. J. Microsc. 213, 1–5. http://dx.doi.org/10.1111/j.1365-2818.2004.01265.x.

Datta, R., Heaster, T.M., Sharick, J.T., Gillette, A.A., Skala, M.C., 2020. Fluorescence lifetime imaging microscopy: fundamentals and advances in instrumentation, analysis, and applications. J. Biomed. Opt. 25, 1–43. http://dx.doi.org/10.1117/1.JBO.25.7.071203.

Digman, M.A., Caiolfa, V.R., Zamai, M., Gratton, E., 2008. The phasor approach to fluorescence lifetime imaging analysis. Biophys. J. 94, L14–L16. http://dx.doi.org/10.1529/biophysj.107.120154.

Gopich, I.V., Szabo, A., 2012. Theory of the energy transfer efficiency and fluorescence lifetime distribution in single-molecule FRET. Proc. Natl. Acad. Sci. U. S. A 109, 7747–7752. http://dx.doi.org/10.1073/pnas.1205120109.

Gregor, I., Patting, M., 2015. Pattern-Based Linear Unmixing for Efficient and Reliable Analysis of Multicomponent TCSPC Data. Springer International Publishing, Cham, pp. 241–263. http://dx.doi.org/10.1007/4243_2014_70.

Kim, J., Park, H., 2009. Toward faster nonnegative matrix factorization: A new algorithm and comparisons. In: Proceedings of the 2008 Eighth IEEE International Conference on Data Mining. ICDM'08, pp. 353–362. http://dx.doi.org/10.1109/ICDM.2008.149.

Laptenok, S., Mullen, K., Borst, J., Stokkum, I.van., Apanasovich, V., Visser, A., 2007. Fluorescence lifetime imaging microscopy (flim) data analysis with timp. J. Stat. Softw. 18, 1–20. http://dx.doi.org/10.18637/jss.v018.i08.

Lee, D.D., Seung, H.S., 2001. Algorithms for non-negative matrix factorization. In: Leen, T.K., Dietterich, T.G., Tresp, V. (Eds.), Advances in Neural Information Processing Systems, Vol. 13. MIT Press, pp. 556–562.

Li, Y., Sapermsap, N., Yu, J., Tian, J., Chen, Y., Li, D.D.U., 2021. Histogram clustering for rapid time-domain fluorescence lifetime image analysis. Biomed. Opt. Express 12, 4293–4307.

Long, Y., Stahl, Y., Weidtkamp-Peters, S., Postma, M., Zhou, W., Goedhart, J., Sánchez-Péez, T.W.J., Simon, R., Scheres, B., Blilou, I., 2017. In vivo fret-flim reveals cell-type-specific protein interactions in arabidopsis roots. Nature 548, 97–102. http://dx.doi.org/10.1038/nature23317.

Margineanu, A., Chan, J.J., Kelly, D.J., Warren, S.C., Flatters, D., Kumar, S., Katan, M., Dunsby, C.W., French, P.M.W., 2016. Screening for protein-protein interactions using fö. Sci. Rep. 6 (28186), http://dx.doi.org/10.1038/srep28186.

Niehörster, T., Löschberger, I., Krämer, H.J., Patting, M., Koberling, F., Enderlein, J., Sauer, M., 2016. Multi-target spectrally resolved fluorescence lifetime imaging microscopy. Nat. Meth. 13 (257), http://dx.doi.org/10.1038/nmeth.3740.

Okabe, K., Inada, N., Gota, C., Harada, Y., Funatsu, T., Uchiyama, S., 2012. Intracellular temperature mapping with a fluorescent polymeric thermometer and fluorescence lifetime imaging microscopy. Nat. Comms. 3 (705), http://dx.doi.org/10.1038/ncomms1714.

Orte, A., Alvarez-Pez, J.M., Ruedas-Rama, M.J., 2013. Fluorescence lifetime imaging microscopy for the detection of intracellular ph with quantum dot nanosensors. ACS Nano 7, 6387–6395. http://dx.doi.org/10.1021/nn402581q.

Raspe, M., Kedziora, K.M., Broek, B.van.den., Zhao, Q., Jong, S.de., Herz, J., Mastop, M., Goedhart, J., Gadella, T.W.J., Young, I.T., Jalink, K., 2016. Siflim: single-image frequency-domain flim provides fast and photon-efficient lifetime data. Nat. Meth. 13 (501), http://dx.doi.org/10.1038/nmeth.3836.

Schmitt, F.J., Thaa, B., Junghans, C., Vitali, M., Veit, M., Friedrich, T., 2014. Egfp-phsens as a highly sensitive fluorophore for cellular ph determination by fluorescence lifetime imaging microscopy (flim). Biochim. Biophys. Acta 1837, 1581–1593. http://dx.doi.org/10.1016/j.bbabio.2014.04.003.

Sinsuebphon, N., Rudkouskaya, A., Barroso, M., Intes, X., 2018. Comparison of illumination geometry for lifetime-based measurements in whole-body preclinical imaging. J. Biophotonics 11, e201800037, URL: https://onlinelibrary.wiley.com/doi/abs/10.1002/jbio.201800037.

Smith, J.T., Yao, R., Sinsuebphon, N., Rudkouskaya, A., Un, N., Mazurkiewicz, J., Barroso, M., Yan, P., Intes, X., 2019. Fast fit-free analysis of fluorescence lifetime imaging via deep learning. Proc. Natl. Acad. Sci. 116, 24019–24030.

Stringari, C., Cinquin, A., Cinquin, O., Digman, M.A., Donovan, P.J., Gratton, E., 2011. Phasor approach to fluorescence lifetime microscopy distinguishes different metabolic states of germ cells in a live tissue. Proc. Natl. Acad. Sci. U.S.A 108, 13582–13587. http://dx.doi.org/10.1073/pnas.1108161108.

Sun, Y., Day, R.N., Periasamy, A., 2011. Investigating protein-protein interactions in living cells using fluorescence lifetime imaging microscopy. Nat. Protocol 6 (1324), http://dx.doi.org/10.1038/nprot.2011.364.

Warren, S.C., Margineanu, A., Alibhai, D., Kelly, D.J., Talbot, C., Alexandrov, Y., Munro, I., Katan, M., Dunsby, C., French, P.M.W., 2013. Rapid global fitting of large fluorescence lifetime imaging microscopy datasets. PLoS One 8, 1–17. http://dx.doi.org/10.1371/journal.pone.0070687.

Wikipedia, The pictures used in this manuscript have been downloaded from Wikipedia, https://commons.wikimedia.org/wiki/File:Michelangelo_-_Creation_of_Adam_(cropped).jpg, https://commons.wikimedia.org/wiki/File:John_Constable_-_The_Hay_Wain_(1821).jpg, https://commons.wikimedia.org/wiki/File:Hans_Holbein_the_Younger_-_The_Ambassadors_-_Google_Art_Project.jpg, https://commons.wikimedia.org/wiki/File:Peter_Paul_Rubens_-_Old_Woman_and_Boy_with_Candles.jpg, https://commons.wikimedia.org/wiki/File:Tsunami_by_hokusai_19th_century.jpg, https://commons.wikimedia.org/wiki/File:Meisje_met_de_parel.jpg, https://commons.wikimedia.org/wiki/File:Venus_botticelli_detail.jpg, https://commons.wikimedia.org/wiki/File:Georges_Seurat_-_A_Sunday_on_La_Grande_Jatte_--_1884_-_Google_Art_Project.jpg, https://commons.wikimedia.org/wiki/File:Monet_Water_Lilies_1916.jpg, https://commons.wikimedia.org/wiki/File:Mona_Lisa,_by_Leonardo_da_Vinci,_from_C2RMF_retouched.jpg, https://commons.wikimedia.org/wiki/File:Van_Gogh_-_Starry_Night_-_Google_Art_Project.jpg, https://commons.wikimedia.org/wiki/File:Agnolo_bronzino-_Ritratto_del_Nano_Morgante_come_bacco_(front)_,_1552,_galleria_Palatina.jpg.

Xiao, D., Chen, Y., Li, D.D.U., 2021. One-dimensional deep learning architecture for fast fluorescence lifetime imaging. IEEE J. Sel. Top. Quantum Electron. 27, 1–10. http://dx.doi.org/10.1109/JSTQE.2021.3049349.